Natural Sciences

RESEARCH ARTICLE

Link between anisotropic electrochemistry and surface transformations at single-crystal silicon electrodes: Implications for lithium-ion batteries

Daniel Martín-Yerga[1,4] | **Mounib Bahri**[2,4] | **Matthew E. Curd**[3,4] |
Xiangdong Xu[1] | **Weiqun Li**[2,4] | **Timothy L. Burnett**[3,4] | **Philip J. Withers**[3,4] |
B. Layla Mehdi[2,4] | **Nigel D. Browning**[2,4] | **Patrick R. Unwin**[1,4]

[1]Department of Chemistry, University of Warwick, Coventry, UK

[2]Department of Mechanical, Materials and Aerospace Engineering, University of Liverpool, Liverpool, UK

[3]Henry Royce Institute, Department of Materials, The University of Manchester, Manchester, UK

[4]The Faraday Institution, Quad One, Harwell Science and Innovation Campus, Didcot, UK

Correspondence
Philip J. Withers, Henry Royce Institute, Department of Materials, The University of Manchester, M13 9PL Manchester, UK.
Email: p.j.withers@manchester.ac.uk

B. Layla Mehdi and Nigel D. Browning, Department of Mechanical, Materials and Aerospace Engineering, University of Liverpool, L69 3GH Liverpool, UK.
Email: blmehdi@liverpool.ac.uk and nigel.browning@liverpool.ac.uk

Patrick R. Unwin, Department of Chemistry, University of Warwick, CV4 7AL Coventry, UK.
Email: p.r.unwin@warwick.ac.uk

Abstract

Silicon is a promising negative electrode material for high-energy-density Li-ion batteries (LiBs) but suffers from significant degradation due to the mechanical stress induced by lithiation. Volume expansion and lithiation in Si are strongly anisotropic but associated early interfacial transformations linked to these phenomena and their implications for electrode performance remain poorly understood. Here we develop a novel correlative electrochemical multi-microscopy approach to study local interfacial degradation at the early stages for three different surface orientations of Si single crystals: Si(1 0 0), Si(1 1 0) and Si(3 1 1), after Li-ion electrochemical cycling. The experimental strategy combines scanning electrochemical cell microscopy (SECCM) measurements with subsequently recorded scanning transmission electron microscopy images of high-quality cross sections of Si electrodes, extracted at selected SECCM regions, using a novel Xe^+ plasma-focused ion beam procedure. These studies reveal significant surface orientation–dependent nanoscale degradation mechanisms that strongly control electrode performance. Si(1 0 0) was immune to interfacial degradation showing the best lithiation reversibility, whereas local nanoscale delamination was observed in Si(1 1 0) leading to a lower Coulombic efficiency. Continuous electrochemical deactivation of Si(3 1 1) was associated with delamination across the whole interface, Li trapping and formation of thick (ca. 60 nm) SiO_2 structures. These results demonstrate surface crystallography to be a critical factor when designing Si-based

battery materials and strongly suggest that promoting Si(1 0 0) facets could potentially provide longer cycling life and performance due to a higher resistance to degradation.

KEYWORDS

correlative microscopy, electrochemistry, li-ion batteries, plasma focused ion beam, scanning electrochemical cell microscopy, scanning transmission electron microscopy, silicon

INTRODUCTION

Li-ion batteries (LiBs) are essential for the decarbonisation of the economy, particularly through the electrification of the transportation system. However, the high demand for electric vehicles with longer ranges requires the use of new chemistries for LiBs with higher specific capacities than prevailing materials. Silicon (Si) provides about 10 times the theoretical specific capacity of graphite and is, therefore, promising as the negative electrode in nonaqueous LiBs.[1–3] However, the use of Si introduces some challenges, such as a large volume expansion during lithiation that leads to mechanical instability,[4,5] a high reactivity of the solid-electrolyte interphase (SEI) that cannot fully passivate the surface to prevent side reactions causing continuous loss of Li^+ and rapid capacity fading,[6–9] and diffusion-controlled lithium trapping.[10,11]

Several strategies have been pursued to circumvent these issues, such as reducing the size of Si particles down to 100 nm to avoid mechanical failure,[12,13] use of nanowires,[14] amorphous Si[15] or heteroatom doping.[11] These studies highlight the importance of understanding how the physicochemical properties of Si materials affect their performance and structural transformations, which is essential to identify design rules for enhanced materials and better batteries. For instance, it is well known that crystalline Si follows a two-phase lithiation reaction with transformation to an amorphous phase during delithiation.[16,17] As a consequence, crystalline Si materials show anisotropic properties in LiBs.[18] Si undergoes anisotropic lithiation and volume expansion, with preferential expansion occurring perpendicular to {1 1 0} planes.[4,19–21] This is believed to occur due to variations in lithium interfacial mobility at different crystallographic planes leading to specific interface-limited reaction rates.[22] Mechanical stresses generated by lithiation and expansion of Si also depend on particle shape and crystallinity[12,13] and thereby are connected to structural instability ultimately leading to crack initiation.[5,13]

Structural degradation of Si electrodes after lithiation/delithiation cycling has been well studied by scanning electron microscopy (SEM), which has allowed visualisation of the appearance of microscale surface cracks[5,23] or the fracture of Si structures.[13] Transmission electron microscopy (TEM) is more suitable for imaging the onset of structural degradation, but the challenges to locate those inherently small defects in extended electrode surfaces have led to TEM studies usually targeting Si electrodes with massive degradation after long-term cycling.[24,25] In situ TEM has enabled the visualisation of crack propagation and fracture in Si nanoparticles with high resolution.[12,26] However, precise control of electrochemistry requires a liquid cell[27,28]; thereby, in situ TEM studies of Si battery materials have mostly focused on the structural evolution without any correlation to changes in electrochemical performance caused by degradation.[4,29,30] Therefore, although cracking and fracture in Si materials is widely assumed to deteriorate battery performance,[31] revealing how degradation at early stages directly affects the electrochemical behaviour has been elusive.

Here, we introduce a novel correlative electrochemical multimicroscopy approach to establish a direct link between the electrochemical response of crystalline Si electrodes for LiBs and transformations of interfacial structure. In recent work, we used scanning electrochemical cell microscopy (SECCM)[32–34] in tandem with shell-isolated nanoparticles for enhanced Raman spectroscopy (SHINERS) to investigate SEI formation at Si(1 1 1) electrodes.[35] Here, we use SECCM to perform local charge/discharge cycling of Si in an Li-ion electrolyte and correlate the responses with changes in interfacial structure visualised by scanning TEM (STEM) at commensurate regions after optimal preparation of high-quality Si cross sections by plasma focused ion beam (p-FIB). We study three distinct monocrystalline electrode orientations – Si(1 0 0), Si(1 1 0) and Si(3 1 1) – which show different electrochemical characteristics and associated degradation pathways that we are able to rationalise. This new way of examining local interfacial processes enabled the identification of nanoscale surface degradation events such as pore formation and delamination at the very early stages, which are connected to poor cycling performance and specific Si crystal orientations.

RESULTS AND DISCUSSION

The correlative multi-microscopy approach is illustrated in Figure 1, with full experimental details in the Supporting Information (SI) section. Briefly, a ca. 1.5 μm diameter pipette probe (Figure S1) filled with 1 M $LiPF_6$ in ethylene carbonate/ethyl methyl carbonate (EC/EMC) was used for SECCM (Figure 1a). The probe was placed sequentially at a series of pre-defined locations on the Si surface by an automated program to carry out spatially resolved electrochemical measurements. The same electrochemical protocol was applied at each location of Si(1 0 0), Si(1 1 0) and Si(3 1 1) electrodes: 10 voltammetric charge/discharge cycles (1 V s^{-1}) between +1.35 V and +0.05 V (vs. Li/Li$^+$) to study lithiation/delithiation processes and the initial stages of the SEI formation (Figure 1b). This approach provides significant statistics as many repetitions ($n = 49$, vide infra) are recorded and allows the identification of any spatial heterogeneity in electrochemical response. SECCM leaves a footprint corresponding to the meniscus (droplet) contact at each analysis point which can be readily identified in SEM images (Figure 1c). As such, selected spots may be extracted as part of a lamella (thin, electron-transparent cross section) using FIB
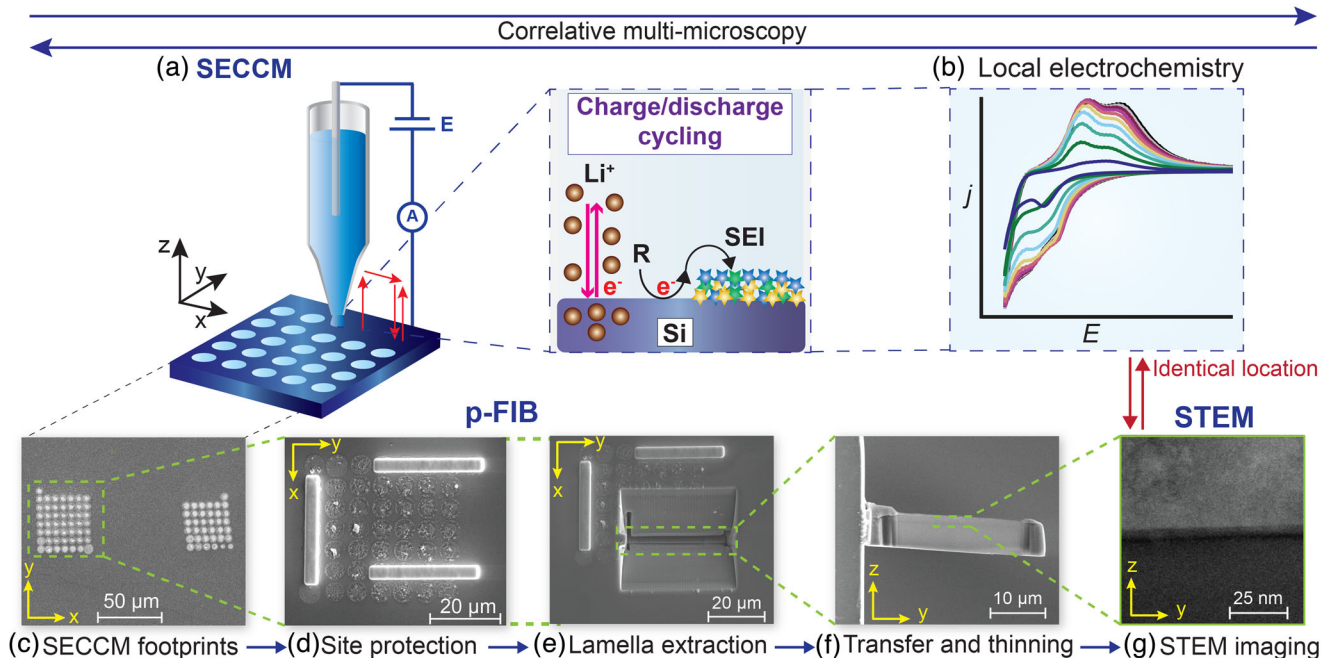
FIGURE 1 Schematic of correlative multi-microscopy workflow incorporating scanning electrochemical cell microscopy (SECCM), plasma-focused ion beam (p-FIB) milling and scanning transmission electron microscopy (STEM): (a) schematic of automated SECCM for spatially resolved charge/discharge cycling at a series of predefined locations on Si electrodes; (b) electrochemical response recorded by SECCM at a specific location of the Si surface; (c) scanning electron microscopy (SEM) image of the footprints left by two different SECCM scans; (d) protection of SECCM sites by deposition of C and Pt/C layers; (e) p-FIB milling of a lamella; (f) transfer and thinning of a lamella for STEM compatibility; (g) STEM imaging of Si interfacial structure at an identical location than the charge/discharge cycling recorded by SECCM in (b).

techniques (Figure 1d–f). This then allows the correlation of nanostructure changes, as revealed by STEM (Figure 1g), with co-located electrochemistry, as revealed by SECCM (Figure 1b).

Preparation of Si cross sections by p-FIB and STEM imaging of pristine Si samples

We developed a novel Xe$^+$ p-FIB approach to prepare high-quality Si cross sections for high-resolution STEM imaging as traditional Ga$^+$ FIB techniques were found to induce various forms of damage into the lamella, including the redeposition of the milled material, implantation of Ga$^+$ ions and amorphization (Figure 2a,b). The amorphized material is typically formed as a layer across the top surface of the lamella, which then impacts upon and compromises the analysis of the SEI and/or Si oxide layers. Use of Xe$^+$ ions is known to substantially reduce the issues associated with Ga$^+$ FIB preparation.[36,37] However, in many cases, a thin (∼10 nm) amorphized layer may remain (Figure 2c), and surface protection by a Pt layer could lead to Pt redeposition on Si (Figure 2d). To address these issues, we modified a known procedure (details in Section S1.3) that entailed initially protecting the Si surface by electron-beam deposition of two thin layers of C and Pt/C before any use of the ion beam. The lamellae were all prepared using an FEI Helios 5 Laser p-FIB system, which is capable of C and mixed-species depositions, unlike many older systems. The deposition of these thin layers ensured no incidental ion damage in the lamella near-surface during Pt deposition and provided better STEM contrast when

visualising the SEI and Si oxide layers relative to Pt. Our modified Xe$^+$ p-FIB approach resulted in Si lamella with no observable amorphization or Pt redeposition (see the consistent lattice structure visible in the high-resolution STEM-high angle annular dark field (HAADF) images in Figures 2f and 3).

This approach was carried out for pristine Si samples of different crystal orientations to visualise the initial surface properties by STEM before SECCM cycling. Protection layers with well-defined boundaries along the interfaces were deposited on Si(1 0 0), Si(1 1 0) and Si(3 1 1) faces as shown in the left-hand images in Figure 3, which demonstrates the high quality of lamellae preparation by p-FIB. Such interfaces and the elemental distribution of Si, C, Pt and O were confirmed on pristine Si(1 0 0) by energy-filtered transmission electron microscopy (EFTEM) imaging in Figure S2. Interfaces for all the Si lamellae are flat and uniform, as shown in Figure 3 (middle), and show the presence of a native oxide layer on top of bulk Si with a thickness of ca. 3 nm (right). Such native oxide layers were confirmed by either electron energy loss spectroscopy (EELS) or EDX mapping of Si(1 0 0), Si(1 1 0) and Si(3 1 1) as shown in Figures S3, S4 and S5, respectively.

Localised electrochemical cycling of Si electrodes by SECCM

SECCM array scans were recorded on the Si(1 0 0), Si(1 1 0) and Si(3 1 1) electrodes under identical conditions, with the average voltammetric profiles for the 1st, 2nd and 10th charge/discharge
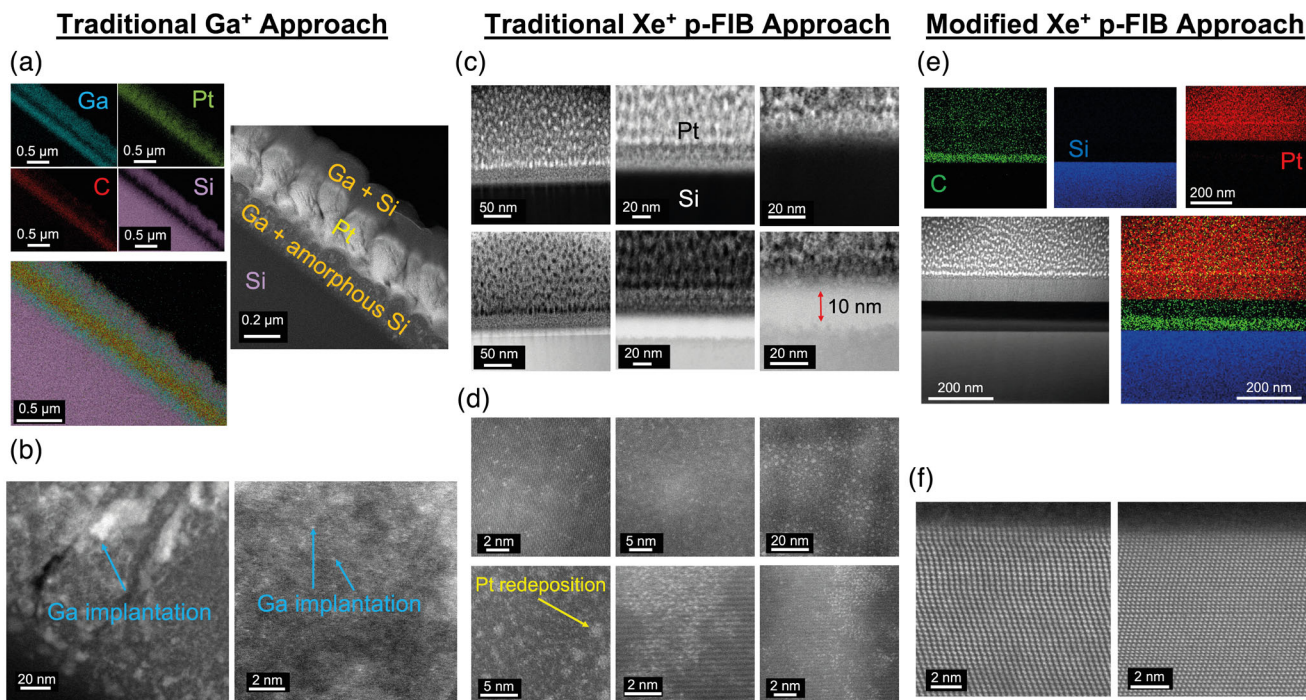
FIGURE 2 Comparison of traditional Ga+ approach (a and b), traditional Xe+ plasma-focused ion beam (p-FIB) approach (c and d) and our modified Xe+ p-FIB approach (e and f) for preparation of Si cross sections: (a) scanning transmission electron microscopy (STEM) energy-dispersive X-ray spectroscopy (EDX) mapping showing Ga, Pt, C and Si distributions with the corresponding STEM-high angle annular dark field (HAADF) image after traditional Ga+ FIB approach; (b) STEM images showing Ga implantation within the Si sample; (c) STEM images showing Pt directly deposited on Si with lower amorphization (ca. 10 nm layer) after traditional Xe+ p-FIB approach; (d) Pt redeposition observed within the Si sample; (e) STEM EDX mapping showing C, Si and Pt distribution with the overlay map and corresponding STEM image after our modified Xe+ p-FIB approach; (f) high-resolution STEM-HAADF images showing the Si interface at atomic resolution without any redeposition and no evidence of amorphisation.

cycle shown in Figure 4a–c (the full 10 cycle sequences are shown in Figure S6). Although we applied a voltammetric scan rate that was several orders of magnitude larger than typically used to study electrochemistry at Si electrodes under LiB conditions, the voltammetric responses, particularly for Si(1 0 0) and Si(1 1 0), were similar to those obtained routinely with more conventional electrochemical experiments at slower scan rates,[5,24] but with some new phenomena observed. These studies add to a growing literature that demonstrates the benefits of employing SECCM at relatively fast scan rates for the investigation of battery electrode materials,[34,35,38,39] facilitated by the relative immunity of SECCM to ohmic effects compared to equivalent macroscopic measurements,[40,41] in part as a consequence of the conical tip geometry and the low overall current magnitudes.

The voltammetric response was rather homogeneous across the 49 points on each of the Si surfaces at this scale (~few μm diameter spots). For Si(1 0 0), two reduction processes in the first charge/discharge cycle are tentatively assigned to electrolyte reduction (R_1) and lithiation (R_2), with a new reduction process (R_3) appearing upon cycling attributed to a second lithiation process. This is the typical response for two-phase lithiation,[18,42,43] entailing lithiation of both the crystalline Si originally present and amorphous Si generated after delithiation of the crystalline phase.[44,45] The increased current density upon cycling, which is seen here, is usually associated with an increased amount of active material after amorphization of Si.[46] Lithiation of the native oxide layer might also occur,[47] particularly in the first cycle, but the contribution of this process to the overall electrochemistry in further cycles should be minimal due to the low thickness of this layer (Figure 3).

On the reverse sweep, two oxidation processes (A_1 and A_2) with increasing current density upon cycling are attributed to the delithiation of two different phases of Li_xSi_y.[18] In general, the peak potential (E_{pa}) was relatively stable for A_1, with A_2 slightly shifting to more positive values upon cycling (Figure S7). Further evidence of the spatially homogeneous response across the Si(1 0 0) surface is provided by representing SECCM data as lithiation (R_2: $j_{lithiation}$ at +0.05 V, Figure 4d) and delithiation (A_2: $j_{delithiation}$ at +0.60 V, Figure 4e) activity maps on Si(1 0 0) with the corresponding SECCM footprint in Figure 4f. Both $j_{lithiation}$ and $j_{delithiation}$ in the first cycle were uniform with a tight distribution of values across the surface (Figure S8). Small differences (ca. 3.0% and 3.4% relative standard deviation for $j_{lithiation}$ and $j_{delithiation}$, respectively) can be ascribed to experimental variability. This spatial homogeneity was largely retained after 10 charge/discharge cycles (Figure S9) with the aforementioned increase in current density.

Anisotropic electrochemistry is evident by comparing the voltammetric profiles of Si(1 0 0), Si(1 1 0) and Si(3 1 1) in Figure 4a–c. Although the first charge/discharge cycle was broadly similar for all
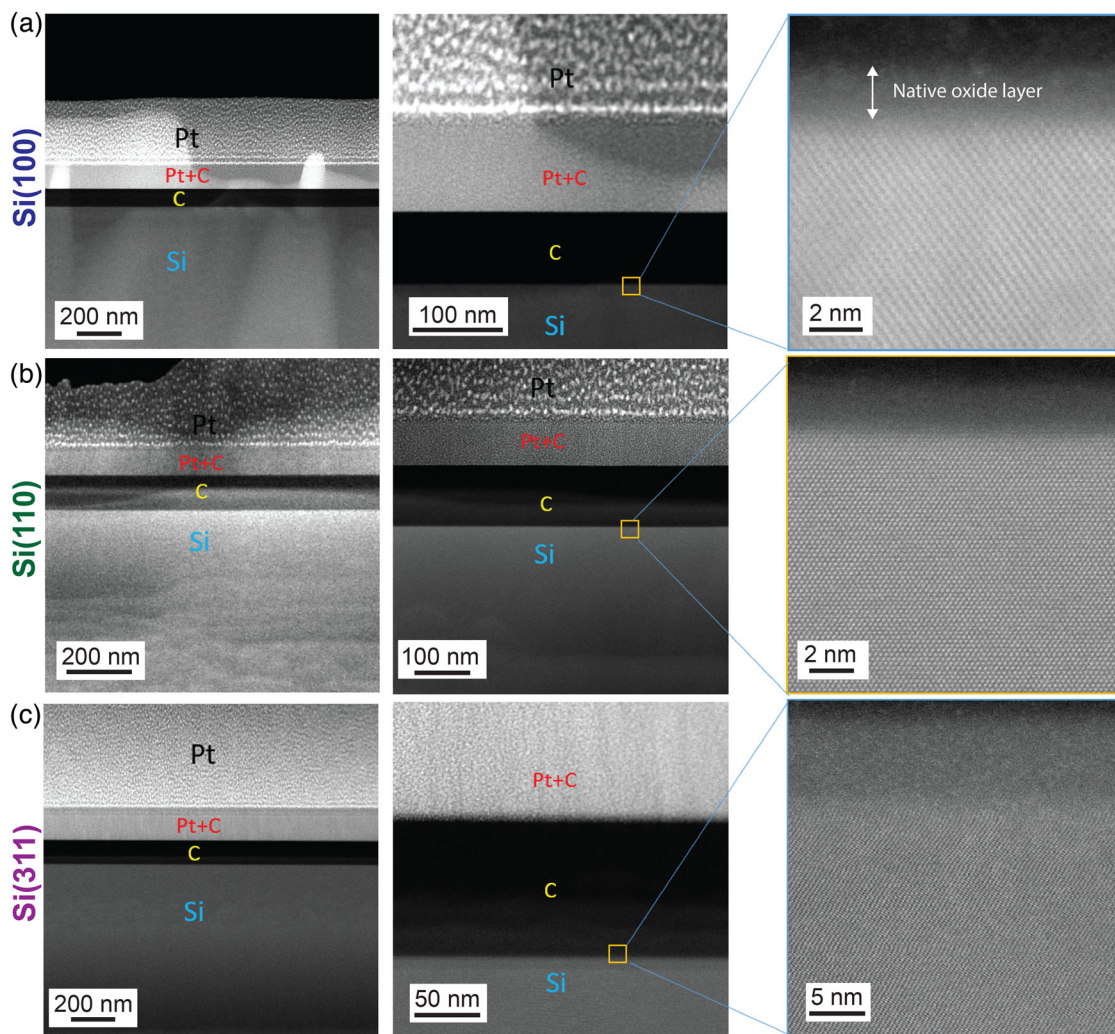
FIGURE 3 Scanning transmission electron microscopy (STEM)-high angle annular dark field (HAADF) images at increasing magnification from left to right showing the morphology and structure of (a) Si(1 0 0), (b) Si(1 1 0) and (c) Si(3 1 1) before electrochemical cycling by scanning electrochemical cell microscopy (SECCM).

orientations, voltammetric profiles evolve very differently for each of the crystal orientations upon cycling (cycle-by-cycle comparison in Figure S10). For instance, Si(1 1 0) shows only one main delithiation process consistently upon cycling (E_{pa} evolution in Figure S7), which might be a consequence of more uniform delithiation kinetics for different Li_xSi_y phases than on Si(1 0 0), leading to voltammetric overlapping or the loss of lithiated silicon (vide infra). In contrast, a completely different cycling behaviour was observed for Si(3 1 1), where reduction currents decreased upon cycling without any significant increase in delithiation current density. Indeed, only a delithiation process could be detected on Si(3 1 1) with relatively low current density that also decreased upon cycling (Figure S11). Interestingly, an additional oxidation process at a peak potential ca. +1.16 V (labelled as A_3 in Figure S11) is tentatively assigned to an Si(3 1 1) surface reaction as the potential is too positive for a delithiation process, and the voltammetric feature also disappeared after the second cycle.

Evolution of reduction (Q_c) and oxidation (Q_a) charges and their ratio (Q_a/Q_c) as a function of cycle number (Figure 4g) is particularly

revealing of the impact of surface structure on charge–discharge characteristics. For both Si(1 0 0) and Si(1 1 0), Q_c and Q_a increased upon cycling, albeit at a faster rate for Si(1 0 0), with the evident trends in Q_c and Q_a suggesting the responses are likely dominated by lithiation and delithiation processes. Interestingly, the Q_a/Q_c ratio sharply increased from first to second cycle (0.33 ± 0.01 to 0.64 ± 0.02 for Si(1 0 0) and 0.081 ± 0.003 to 0.200 ± 0.008 for Si(1 1 0)), which can be associated with the initial SEI formation providing partial surface passivation that minimises electrolyte reduction in successive cycles. The Q_a/Q_c ratio was significantly higher for Si(1 0 0) compared with Si(1 1 0), which indicates either more reversible lithiation/delithiation via the Si(1 0 0) surface, or lower stability of the initial SEI on Si(1 1 0) leading to a more reactive surface for side reactions.

Q_a/Q_c was still growing, if only modestly, during the last (8th–10th) cycles, which demonstrates the occurrence of side processes during cycling, and that the interface has not reached a steady state. Indeed, Q_a/Q_c ratio was 0.87 ± 0.01 and 0.45 ± 0.03 for Si(1 0 0) and Si(1 1 0) at the 10th cycle, respectively, still far from full charge/discharge
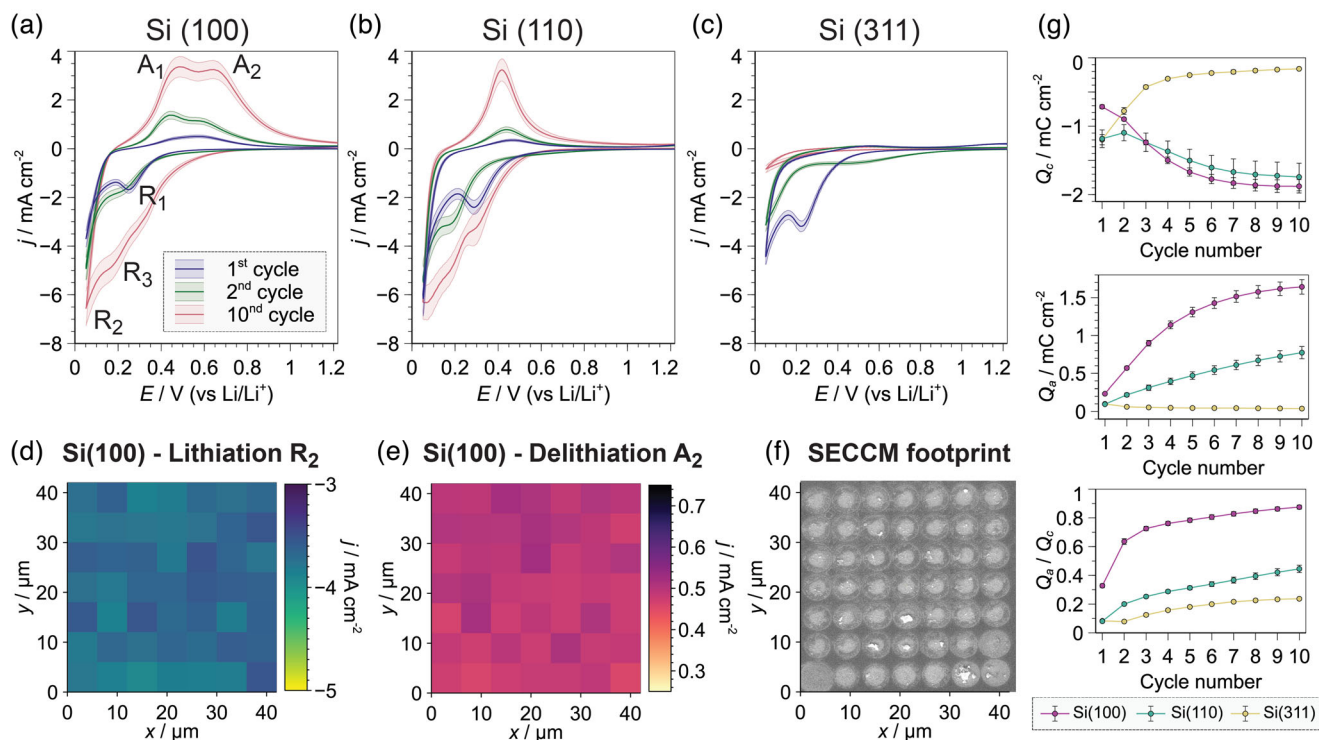
FIGURE 4 Average scanning electrochemical cell microscopy (SECCM) cyclic voltammograms ($n = 49$) for the 1st, 2nd and 10th charge/discharge cycles in 1 M LiPF$_6$ in EC/EMC recorded at 1 V s^{-1} at (a) Si(1 0 0), (b) Si(1 1 0) and (c) Si(3 1 1); (d) lithiation and (e) delithiation maps of Si(1 0 0) representing the current densities recorded at +0.05 V (*forward*) and +0.60 V (*reverse*) versus Li/Li$^+$, respectively; (f) scanning electron microscopy (SEM) image of the corresponding footprint left by the SECCM array on Si(1 0 0); (g) evolution of cathodic (Q_c), anodic (Q_a) and Q_a/Q_c ratio as a function of charge/discharge cycle for the Si(1 0 0), Si(1 1 0) and Si(3 1 1) surface orientations.

reversibility. Transient increases in Coulombic efficiency during these initial charge/discharge cycles are common with Si electrodes due to the well-known instability and breathing effect of the SEI layer.[7,48] This leads to its continuous formation, which has been identified as the main mechanism for lithium loss in Si-based LiBs.[49]

In stark contrast to the above, the magnitude (in absolute value) of both Q_c and Q_a decrease markedly upon cycling for Si(3 1 1). This suggests the loss of electrochemical activity of the Si surface: Q_c from -1.20 ± 0.08 mC cm^{-2} (1st cycle) to -0.16 ± 0.01 mC cm^{-2} (10th cycle) and Q_a from 0.100 ± 0.007 mC cm^{-2} (1st cycle) to 0.038 ± 0.002 mC cm^{-2} (10th cycle). This particular behaviour led to a very low Q_a/Q_c ratio during the whole experiment (0.237 ± 0.006 at 10th cycle), which reaffirms the relatively poor performance of Si(3 1 1) as an LiB electrode compared to Si(1 0 0) and Si(1 1 0). Although Si(3 1 1) is not a common electrode orientation, {3 1 1} defects can form during ion implantation and annealing conditions relevant to Si processing[50] and thus might be accessible to electrolytes in battery materials.

Correlative STEM imaging of cycled Si interfaces

Correlative STEM was conducted after SECCM to study the morphology and structure of Si interfaces and gain further understanding of

the anisotropic performance among Si(1 0 0), Si(1 1 0) and Si(3 1 1). Although the interfaces of pristine Si(1 0 0), Si(1 1 0) and Si(3 1 1) had similar morphology and structure, clear anisotropic differences were identified after electrochemical cycling by SECCM (ending at a discharged state). The most noticeable interfacial transformations were the formation of the SEI layer and changes in surface roughness compared to the pristine state, observed for all three Si samples. Average thickness of the SEI layers were 170 ± 5 nm [Si(1 0 0)], 210 ± 10 nm [Si(1 1 0)] and 140 ± 10 nm [Si(3 1 1)], respectively, estimated from STEM, EFTEM and EELS imaging (vide infra). The SEI/Si interface on Si(1 0 0) was still flat and compact after SECCM cycling, as shown in Figure 5a–c, consistent with Si(1 0 0) providing good cyclability and electrochemical performance as previously discussed. EFTEM images (Figure S12) show the elemental distribution on cycled Si(1 0 0). The high O concentration at the SEI/Si interface suggests the presence of the native Si oxide layer even after cycling. The SEI layer contained Li, F, C and O, also confirmed by EELS mapping near the SEI/Si interface, as shown in Figure S13. Both Li and F accumulated near the SEI/Si interface in contrast to C that was more concentrated away from this interface. This observation is consistent with the bilayer SEI model,[6,51] where the inner layer is enriched in inorganic species such as LiF, whereas organic species mostly form the top layers of the SEI. Some small defects such as pores and cavities were also observed in the SEI layer, highlighted by the green arrows in Figure 5a. These nanoscale
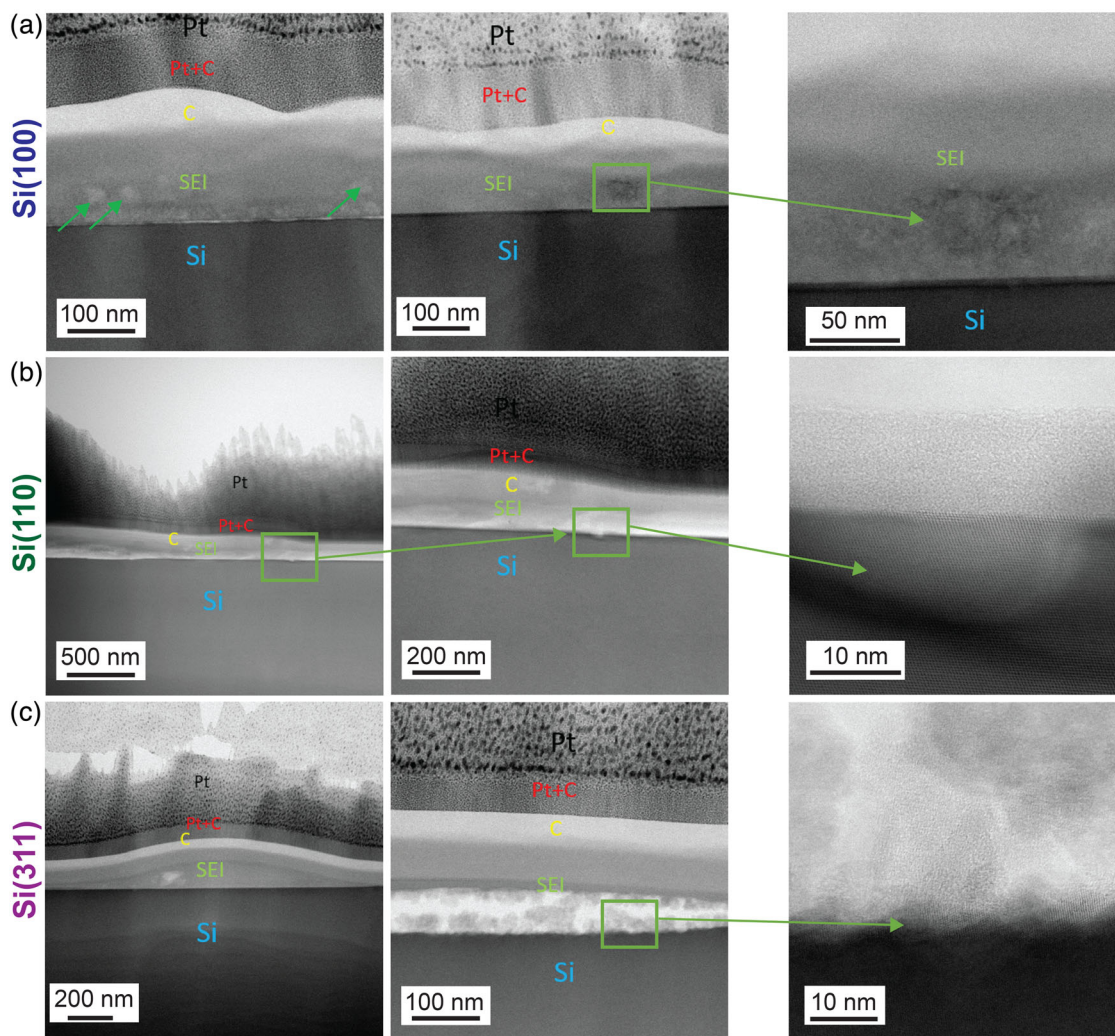
FIGURE 5 Scanning transmission electron microscopy (STEM)–brightfield (BF) images at increasing magnification from left to right showing the morphology and structure of (a) Si(1 0 0), (b) Si(1 1 0) and (c) Si(3 1 1) after 10 charge/discharge electrochemical cycles by scanning electrochemical cell microscopy (SECCM).

defects, exposing the Si electrode to the electrolyte, are likely to be sites for further electrolyte reactivity and thus associated with a Coulombic efficiency lower than 1, as measured at 10 charge/discharge cycles (Q_a/Q_c of 0.87). Figure S14 shows a comparison between the Si(1 0 0) interface before and after SECCM, including atomic resolution imaging and electron diffraction pattern analysis. The pristine sample (Figure S14a) shows different atomic planes of Si with the zone axis orientation of [1 1 0] as determined by simulated electron diffraction. After cycling, the corresponding diffraction pattern has the typical layered pattern (yellow arrows in Figure S14b), which confirms the insertion of Li without creating any significant interfacial defects as for the other Si orientations (vide infra). The observation of this lithiated phase also suggests some Li trapping on Si(1 0 0) that might contribute to the measured Coulombic efficiency because the imaging was carried out at a discharged state.

SECCM cycling of Si(1 1 0) produced an even greater abundance of local defects at the SEI/Si interface, such as delamination (Figure 5b). Higher resolution STEM imaging in Figure 5b shows the formation of pores at a location where delamination also occurred, with a relatively large pore size of around 20–30 nm. Some of the Si lattices are still observed as the pore size was smaller than the thickness of the lamella. EELS mapping in Figure S15a shows the elemental distribution near the local delamination site; F and O are enhanced near the SEI/Si interface, whereas a higher concentration of C was detected away from this interface (carbonaceous species mostly present on the uppermost SEI layers). Although the entry of Li ions into Si occurs perpendicular to the surface, lateral Li transport is most likely inducing the observed delamination.[13] Microscale delamination has been widely observed when cracks propagate in the vertical direction and are then deflected laterally,[5,13] which occurs gradually with insignificant damage during the first few cycles. Our findings demonstrate that delamination can also occur through nanoscale cracking at the Si interface and at the very earliest stages of lithiation. These degradation events share similarities with the atomic layer-by-layer peeling observed at {1 1 1} facets during lithiation at the reaction front between amorphous Li_xSi and crystalline Si.[52] This deeper degradation of Si(1 1 0) compared

to Si(100) supports the SECCM observation of a lower cycling performance for Si(110). Additional STEM images in Figure S15b show further pores and delamination sites on the Si(110) interface with atomic resolution.

Si(311) showed even greater interfacial degradation after SECCM cycling (Figure 5c). The SEI/Si interface was bulged and formed a wavy and zigzag-like structure, associated with the large volume change and mechanical stresses along this surface orientation upon cycling. Such morphological transformations in Si surfaces upon electrochemical cycling have been previously reported.[24,53] Multiple cracking and delamination on the Si(311) interface led to a fast decay of electrochemical performance with low lithiation reversibility during SECCM (vide supra). The poor lithiation reversibility suggests that degradation takes place on Li_xSi, which would be irreversibly lost and unavailable for delithiation. Additionally, EELS mapping (Figure S16a) shows the formation of a relatively thick (ca. 60 nm) SiO_2 layer at the SEI/Si interface, which may contribute to blocking Li transport pathways and poor electrical conductivity during electrochemical cycling. SiO_2 generation could be related to the specific anodic process detected on Si(311) at the first cycle shown in Figure S11, which was absent on Si(100) and Si(110). In turn, this could then be responsible for the subsequently different electrochemistry after the first cycle for Si(311). It is, however, difficult to unambiguously determine the specific process leading to the formation of this SiO_2 layer. High-resolution STEM images in Figure S16b show the atomic scale Si interfacial structure with various orientations, which was caused by volume and morphological changes induced by cycling. The diffraction patterns showed the presence of a mixture of Si and Li_xSi_y that might indicate Li trapping on the Si(311) surface as an additional contribution to the low electrochemical reversibility observed.

CONCLUSIONS

In summary, a novel correlative electrochemical multi-microscopy approach has been developed to study interfacial degradation at early stages in Si single-crystal electrodes, under conditions relevant to Li-ion cells. Local electrochemical cycling and co-located interfacial imaging at the precise locations where electrochemistry is measured of three independent Si surface orientations, namely Si(100), Si(110) and Si(311), revealed a strong link between anisotropic cycling performance and nanoscale degradation phenomena. Si(100) showed overall the best lithiation reversibility (i.e. Coulombic efficiency) and a stable, homogeneous and degradation-free interface after cycling. The Coulombic efficiency was significantly lower for Si(110), which is ascribed to the localised formation of nanoscale pores by delamination of lithiated material (Li_xSi_y). Si(311) suffered from general interfacial deterioration, Li trapping and formation of thick SiO_2 structures, all of which contribute to a very low reversibility and continuous decrease of electrochemical activity upon cycling. Based on these observations that unambiguously link the early stages of interfacial degradation and cycling performance, we identify surface crystallography as a critical factor to consider when designing more stable Si-based LiBs. Indeed,

our results suggest that the Si(100) orientation should be promoted in materials used for this kind of battery to increase cycle life and performance. Further, our novel correlative imaging approach opens future avenues for elucidating structure–activity–degradation relationships at the very early stages across a variety of battery materials beyond silicon and lithium ion. Our approach is compelling not only because it provides a means to link structure-electrochemical activity changes directly in the same microscopic locations, but also because multiple such measurements can be made across a surface to create large, statistically robust datasets.

CONFLICT OF INTEREST STATEMENT

The authors declare no conflicts of interest.

DATA AVAILABILITY STATEMENT

The data that support the findings of this study are openly available in Zenodo at http://doi.org/10.5281/zenodo.7503802.

ETHICS STATEMENT

The authors confirm that they have followed the ethical policies of the journal.

ORCID

Daniel Martín-Yerga https://orcid.org/0000-0002-9385-7577
Mounib Bahri https://orcid.org/0000-0002-8336-9158
Xiangdong Xu https://orcid.org/0000-0002-1120-4661
Weiqun Li https://orcid.org/0000-0003-1325-9807
Timothy L. Burnett https://orcid.org/0000-0002-6896-0839
Philip J. Withers https://orcid.org/0000-0002-1946-5647

B. Layla Mehdi https://orcid.org/0000-0002-8281-9524
Nigel D. Browning https://orcid.org/0000-0003-0491-251X
Patrick R. Unwin https://orcid.org/0000-0003-3106-2178

PEER REVIEW

The peer review history for this article is available at https://publons.com/publon/10.1002/ntls.20210607.

REFERENCES

1. Feng K, Li M, Liu W, et al. Silicon-based anodes for lithium-ion batteries: from fundamentals to practical applications. *Small.* 2018;14(8):1702737. https://doi.org/10.1002/smll.201702737
2. Cui Y. Silicon anodes. *Nat Energy.* 2021;6(10):995-996. https://doi.org/10.1038/s41560-021-00918-2
3. Zuo X, Zhu J, Müller-Buschbaum P, Cheng YJ. Silicon based lithium-ion battery anodes: a chronicle perspective review. *Nano Energy.* 2017;31:113-143. https://doi.org/10.1016/j.nanoen.2016.11.013
4. Liu XH, Zheng H, Zhong L, et al. Anisotropic swelling and fracture of silicon nanowires during lithiation. *Nano Lett.* 2011;11(8):3312-3318. https://doi.org/10.1021/nl201684d
5. Shi F, Song Z, Ross PN, Somorjai GA, Ritchie RO, Komvopoulos K. Failure mechanisms of single-crystal silicon electrodes in lithium-ion batteries. *Nat Commun.* 2016;7(1):11886. https://doi.org/10.1038/ncomms11886
6. Kim J, Chae OB, Lucht BL. Perspective—structure and stability of the solid electrolyte interphase on silicon anodes of lithium-ion batteries. *J Electrochem Soc.* 2021;168(3):030521. https://doi.org/10.1149/1945-7111/abe984
7. Hasa I, Haregewoin AM, Zhang L, et al. Electrochemical reactivity and passivation of silicon thin-film electrodes in organic carbonate electrolytes. *ACS Appl Mater Interfaces.* 2020;12(36):40879-40890. https://doi.org/10.1021/acsami.0c09384
8. Huang W, Wang J, Braun MR, et al. Dynamic structure and chemistry of the silicon solid-electrolyte interphase visualized by cryogenic electron microscopy. *Matter.* 2019;1(5):1232-1245. https://doi.org/10.1016/j.matt.2019.09.020
9. Yoon I, Abraham DP, Lucht BL, Bower AF, Guduru PR. In situ measurement of solid electrolyte interphase evolution on silicon anodes using atomic force microscopy. *Adv Energy Mater.* 2016;6(12):1600099. https://doi.org/10.1002/aenm.201600099
10. Rehnlund D, Lindgren F, Böhme S, et al. Lithium trapping in alloy forming electrodes and current collectors for lithium based batteries. *Energy Environ Sci.* 2017;10(6):1350-1357. https://doi.org/10.1039/C7EE00244K
11. Zhu B, Liu G, Lv G, et al. Minimized lithium trapping by isovalent isomorphism for high initial Coulombic efficiency of silicon anodes. *Sci Adv.* 2019;5(11):eaax0651. https://doi.org/10.1126/sciadv.aax0651
12. Liu XH, Zhong L, Huang S, Mao SX, Zhu T, Huang JY. Size-dependent fracture of silicon nanoparticles during lithiation. *ACS Nano.* 2012;6(2):1522-1531. https://doi.org/10.1021/nn204476h
13. Lee SW, McDowell MT, Berla LA, Nix WD, Cui Y. Fracture of crystalline silicon nanopillars during electrochemical lithium insertion. *Proc Natl Acad Sci.* 2012;109(11):4080-4085. https://doi.org/10.1073/pnas.1201088109
14. Chan CK, Peng H, Liu G, et al. High-performance lithium battery anodes using silicon nanowires. *Nat Nanotechnol.* 2008;3(1):31-35. https://doi.org/10.1038/nnano.2007.411
15. Lin L, Xu X, Chu C, Majeed MK, Yang J. Mesoporous amorphous silicon: a simple synthesis of a high-rate and long-life anode material for lithium-ion batteries. *Angew Chem Int Ed.* 2016;55(45):14063-14066. https://doi.org/10.1002/anie.201608146
16. Key B, Morcrette M, Tarascon JM, Grey CP. Pair distribution function analysis and solid state NMR studies of silicon electrodes for lithium ion batteries: understanding the (de)lithiation mechanisms. *J Am Chem Soc.* 2011;133(3):503-512. https://doi.org/10.1021/ja108085d
17. Liu XH, Zhang LQ, Zhong L, et al. Ultrafast electrochemical lithiation of individual Si nanowire anodes. *Nano Lett.* 2011;11(6):2251-2258. https://doi.org/10.1021/nl200412p
18. McDowell MT, Lee SW, Nix WD, Cui Y. 25th anniversary article: understanding the lithiation of silicon and other alloying anodes for lithium-ion batteries. *Adv Mater.* 2013;25(36):4966-4985. https://doi.org/10.1002/adma.201301795
19. Lee SW, McDowell MT, Choi JW, Cui Y. Anomalous shape changes of silicon nanopillars by electrochemical lithiation. *Nano Lett.* 2011;11(7):3034-3039. https://doi.org/10.1021/nl201787r
20. Goldman JL, Long BR, Gewirth AA, Nuzzo RG. Strain anisotropies and self-limiting capacities in single-crystalline 3D silicon microstructures: models for high energy density lithium-ion battery anodes. *Adv Funct Mater.* 2011;21(13):2412-2422. https://doi.org/10.1002/adfm.201002487
21. Yuk JM, Seo HK, Choi JW, Lee JY. Anisotropic lithiation onset in silicon nanoparticle anode revealed by *in situ* graphene liquid cell electron microscopy. *ACS Nano.* 2014;8(7):7478-7485. https://doi.org/10.1021/nn502779n
22. Yang H, Huang S, Huang X, et al. Orientation-dependent interfacial mobility governs the anisotropic swelling in lithiated silicon nanowires. *Nano Lett.* 2012;12(4):1953-1958. https://doi.org/10.1021/nl204437t
23. Sternad M, Forster M, Wilkening M. The microstructure matters: breaking down the barriers with single crystalline silicon as negative electrode in Li-ion batteries. *Sci Rep.* 2016;6(1):31712. https://doi.org/10.1038/srep31712
24. Lau D, Hall CA, Lim S, et al. Reduced silicon fragmentation in lithium ion battery anodes using electronic doping strategies. *ACS Appl Energy Mater.* 2020;3(2):1730-1741. https://doi.org/10.1021/acsaem.9b02200
25. Domi Y, Usui H, Yamaguchi K, Yodoya S, Sakaguchi H. Silicon-based anodes with long cycle life for lithium-ion batteries achieved by significant suppression of their volume expansion in ionic-liquid electrolyte. *ACS Appl Mater Interfaces.* 2019;11(3):2950-2960. https://doi.org/10.1021/acsami.8b17123
26. Lee SW, Lee HW, Ryu I, Nix WD, Gao H, Cui Y. Kinetics and fracture resistance of lithiated silicon nanostructure pairs controlled by their mechanical interaction. *Nat Commun.* 2015;6(1):7533. https://doi.org/10.1038/ncomms8533
27. Gu M, Parent LR, Mehdi BL, et al. Demonstration of an electrochemical liquid cell for operando transmission electron microscopy observation of the lithiation/delithiation behavior of Si nanowire battery anodes. *Nano Lett.* 2013;13(12):6106-6112. https://doi.org/10.1021/nl403402q
28. Mehdi BL, Qian J, Nasybulin E, et al. Observation and quantification of nanoscale processes in lithium batteries by operando electrochemical (S)TEM. *Nano Lett.* 2015;15(3):2168-2173. https://doi.org/10.1021/acs.nanolett.5b00175
29. Gu M, Li Y, Li X, et al. *In situ* TEM study of lithiation behavior of silicon nanoparticles attached to and embedded in a carbon matrix. *ACS Nano.* 2012;6(9):8439-8447. https://doi.org/10.1021/nn303312m
30. McDowell MT, Lee SW, Harris JT, et al. In situ TEM of two-phase lithiation of amorphous silicon nanospheres. *Nano Lett.* 2013;13(2):758-764. https://doi.org/10.1021/nl3044508
31. Gu M, He Y, Zheng J, Wang C. Nanoscale silicon as anode for Li-ion batteries: the fundamentals, promises, and challenges. *Nano Energy.* 2015;17:366-383. https://doi.org/10.1016/j.nanoen.2015.08.025
32. Ebejer N, Schnippering M, Colburn AW, Edwards MA, Unwin PR. Localized high resolution electrochemistry and multifunctional imaging: scanning electrochemical cell microscopy. *Anal Chem.* 2010;82(22):9141-9145. https://doi.org/10.1021/ac102191u
33. Bentley CL, Kang M, Unwin PR. Scanning electrochemical cell microscopy: new perspectives on electrode processes in action.

Curr Opin Electrochem. 2017;6(1):23-30. https://doi.org/10.1016/j.coelec.2017.06.011

34. Martín-Yerga D, Kang M, Unwin PR. Scanning electrochemical cell microscopy in a glovebox: structure-activity correlations in the early stages of solid-electrolyte interphase formation on graphite. *ChemElectroChem.* 2021;8(22):4240-4251. https://doi.org/10.1002/celc.202101161

35. Martín-Yerga D, Milan DC, Xu X, et al. Dynamics of solid-electrolyte interphase formation on silicon electrodes revealed by combinatorial electrochemical screening. *Angew Chem Int Ed.* 2022;61(34):e202207184. https://doi.org/10.1002/anie.202207184

36. Burnett TL, Kelley R, Winiarski B, et al. Large volume serial section tomography by Xe Plasma FIB dual beam microscopy. *Ultramicroscopy.* 2016;161:119-129. https://doi.org/10.1016/j.ultramic.2015.11.001

37. Zhong X, Wade CA, Withers PJ, et al. Comparing Xe$^+$ pFIB and Ga$^+$ FIB for TEM sample preparation of Al alloys: minimising FIB-induced artefacts. *J Microsc.* 2021;282(2):101-112. https://doi.org/10.1111/jmi.12983

38. Tetteh EB, Valavanis D, Daviddi E, et al. Fast Li-ion storage and dynamics in TiO$_2$ nanoparticle clusters probed by smart scanning electrochemical cell microscopy. *Angew Chem Int Ed.* 2023;62(9):e202214493. https://doi.org/10.1002/anie.202214493

39. Tao B, McPherson IJ, Daviddi E, Bentley CL, Unwin PR. Multiscale electrochemistry of lithium manganese oxide (LiMn$_2$O$_4$): from single particles to ensembles and degrees of electrolyte wetting. *ACS Sustain Chem Eng.* 2023;11(4):1459-1471. https://doi.org/10.1021/acssuschemeng.2c06075

40. Wahab OJ, Kang M, Meloni GN, Daviddi E, Unwin PR. Nanoscale visualization of electrochemical activity at indium tin oxide electrodes. *Anal Chem.* 2022;94(11):4729-4736. https://doi.org/10.1021/acs.analchem.1c05168

41. Daviddi E, Chen Z, Beam Massani B, et al. Nanoscale visualization and multiscale electrochemical analysis of conductive polymer electrodes. *ACS Nano.* 2019;13(11):13271-13284. https://doi.org/10.1021/acsnano.9b06302

42. Obrovac MN, Krause LJ. Reversible cycling of crystalline silicon powder. *J Electrochem Soc.* 2007;154(2):A103. https://doi.org/10.1149/1.2402112

43. Wang JW, He Y, Fan F, et al. Two-phase electrochemical lithiation in amorphous silicon. *Nano Lett.* 2013;13(2):709-715. https://doi.org/10.1021/nl304379k

44. Iaboni DSM, Obrovac MN. Li$_{15}$Si$_4$ formation in silicon thin film negative electrodes. *J Electrochem Soc.* 2016;163(2):A255-A261. https://doi.org/10.1149/2.0551602jes

45. McDowell MT, Ryu I, Lee SW, Wang C, Nix WD, Cui Y. Studying the kinetics of crystalline silicon nanoparticle lithiation with in situ transmission electron microscopy. *Adv Mater.* 2012;24(45):6034-6041. https://doi.org/10.1002/adma.201202744

46. Schroder KW, Dylla AG, Harris SJ, Webb LJ, Stevenson KJ. Role of surface oxides in the formation of solid–electrolyte interphases at silicon electrodes for lithium-ion batteries. *ACS Appl Mater Interfaces.* 2014;6(23):21510-21524. https://doi.org/10.1021/am506517j

47. Cao C, Abate II, Sivonxay E, et al. Solid electrolyte interphase on native oxide-terminated silicon anodes for Li-ion batteries. *Joule.* 2019;3(3):762-781. https://doi.org/10.1016/j.joule.2018.12.013

48. Jin Y, Li S, Kushima A, et al. Self-healing SEI enables full-cell cycling of a silicon-majority anode with a Coulombic efficiency exceeding 99.9%. *Energy Environ Sci.* 2017;10(2):580-592. https://doi.org/10.1039/C6EE02685K

49. Haufe S, Bernhard R, Pfeiffer J. Revealing the failure mechanism of partially lithiated silicon-dominant anodes based on microscale silicon particles. *J Electrochem Soc.* 2021;168(8):080531. https://doi.org/10.1149/1945-7111/ac1491

50. Marqués LA, Aboy M, Dudeck KJ, Botton GA, Knights AP, Gwilliam RM. Modeling and experimental characterization of stepped and v-shaped {311} defects in silicon. *J Appl Phys.* 2014;115(14):143514. https://doi.org/10.1063/1.4871538

51. Stetson C, Schnabel M, Li Z, et al. Microscopic observation of solid electrolyte interphase bilayer inversion on silicon oxide. *ACS Energy Lett.* 2020;5(12):3657-3662. https://doi.org/10.1021/acsenergylett.0c02081

52. Liu XH, Wang JW, Huang S, et al. In situ atomic-scale imaging of electrochemical lithiation in silicon. *Nat Nanotechnol.* 2012;7(11):749-756. https://doi.org/10.1038/nnano.2012.170

53. Stetson C, Yin Y, Norman A, et al. Evolution of solid electrolyte interphase and active material in the silicon wafer model system. *J Power Sources.* 2021;482:228946. https://doi.org/10.1016/j.jpowsour.2020.228946

SUPPORTING INFORMATION

Additional supporting information can be found online in the Supporting Information section at the end of this article.

How to cite this article: Martín-Yerga D, Bahri M, Curd ME, et al. Link between anisotropic electrochemistry and surface transformations at single-crystal silicon electrodes: Implications for lithium-ion batteries. *Nat Sci.* 2023;e20210607. https://doi.org/10.1002/ntls.20210607